Electronic Supplementary Material (ESI) for Journal of Materials Chemistry C.

Supporting Information

Anisotropic Thermally Conductive Flexible Films based on Nanofibrillated Cellulose and Aligned Graphene Nanosheets

Na Song*‡, Dejin Jiao‡, Peng Ding*, Siqi Cui, Shengfu Tang, Liyi Shi

Research Center of Nanoscience and Nanotechnology, Shanghai University, 99 Shangda Road, Shanghai 200444, China

1. Experimental Section

Synthesis of GO. GO was synthesized from natural graphite powder using a modified Hummer's method.[1] Briefly, graphite powder (4 g) was placed in a flask. Concentrated H_2SO_4 (92 mL) was added slowly while stirring in an ice bath. Subsequently, $KMnO_4$ (12 g) was added gradually over 1 h while stirring, and the temperature of the mixed solution was maintained at 0 °C. After stirring vigorously for another 15 min at room temperature, the mixture was heated to 35 °C and continuously stirred for 2 h. Then, the mixture was diluted with deionized (DI) water (184 mL) and stirred for 15 min. Subsequently, DI water (280 mL) was added, followed by the drop-wise addition of H_2O_2 (10 mL). The suspension was vacuum-filtered and washed with HCl solution (1:10), and it was successively washed with DI water for more than 15 times until a pH of 7 was obtained. The filter cake was re-dispersed in water and sonicated for 1 h. After centrifugation at 5000 rpm for 5 min, a yellowish-brown GO dispersion was obtained.

Synthesis of the NFC suspension. The NFC dispersion was prepared according to the method reported by Saito.[2] Cellulose fibers (2 g of cellulose content) were suspended in DI water (200 mL) that contained TEMPO (0.025 g) and NaBr (0.25 g). The oxidation reaction of the cellulose slurry was initiated by adding the desired amount of the NaClO solution (10 mmol•g^{-1} cellulose), and the reaction continued at room temperature with stirring. The pH of the reaction solution was maintained at 10 by adding 0.5 M of NaOH

for 6 h. The oxidized cellulose was thoroughly washed with DI water by filtration on a filter membrane (PTFE, 0.45 μm). Subsequently, 2 mg•mL^{-1} of the oxidized cellulose/water slurries were sonicated for 15 min at a power of 300 W in an ice bath using an ultrasonic generator with a probe tip that had a diameter of 15 cm. Then, the slurry was centrifuged at 8000 rpm for 10 min to remove the un-nanofibrillated cellulose. The transparent NFC suspension was stored at 4 °C before use.

Preparation of the NFC/RGO hybrid films using a two-step approach. The as-made GO dispersion was diluted to 1 mg•mL^{-1}. Approximately 0.2 mL of hydrazine was added to 100 mL of the diluted GO dispersion, and the reaction was maintained for 2 h at 95 °C. After cooling to room temperature, the dispersion was vacuum-filtered, and the residue was washed with sufficient DI water to eliminate the impurities. Subsequently, a certain amount of filter residue was re-dispersed in DI water. The RGO dispersions were added to the NFC suspensions at room temperature and then sonicated for 10 min. After vigorously stirring for approximately 2 h, the hybrid dispersion was vacuum-filtered on a mixed cellulose ester membrane (47 mm in diameter, 0.45 μm pore size) and washed with sufficient DI water to eliminate the impurities. The films were dried in a vacuum oven at 40 °C overnight before removing the hybrid films from the membranes. The hybrid film with NFC/GO had a weight ratio of 95:5.

Preparation of the NFC/GO hybrid films. GO dispersions were controllably added to the NFC suspensions at room temperature and then vigorously stirred for

approximately 30 min to yield a homogeneous dispersion with a graphene content of 5 wt% and 20 wt% relative to the NFC (total solids of 100 mg in 100 mL DI water). The reactions were heated to 95 °C and stirred for 2 h to coordinate the reaction conditions with the NFC/GO hybrid films. After cooling to room temperature, the dispersion was vacuum-filtered on a mixed cellulose ester membrane (47 mm in diameter, 0.45 μm pore size) and washed with sufficient DI water to eliminate impurities. The films were dried in a vacuum oven at 60 °C overnight before removing the hybrid films from the membranes. The hybrid films with a NFC/GO weight ratio of 80:20 were named CGO-20.

2. Schematic representation of the preparation of the hybrid films

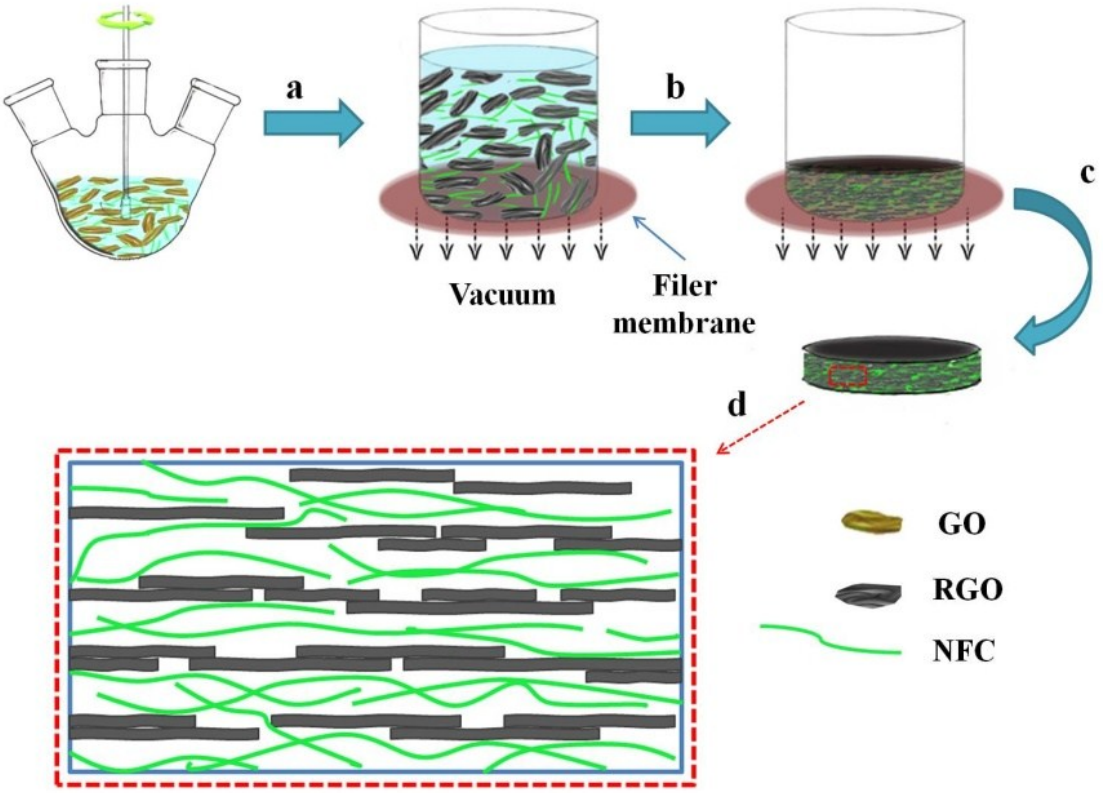

Figure S1. Schematic representation of the preparation of the hybrid films. (a) In situ reduction. (b) Vaccum-filtration. (c) Dry and obtain the hybrid films. (d) Schematic diagram of the transversal surface of hybrid films.

3. In situ reduction of GO to RGO

The in situ reduction of GO to RGO was confirmed using FTIR, XRD, Raman and TGA. For comparison, RGO and NFC/GO hybrid films (CGO-20) were also prepared. Figure S2 displays the FTIR spectra of GO, RGO, CG0, CG20 and CGO-20. The FTIR spectrum of GO showed several absorption peaks at 1054, 1221, 1402, 1625, 1726 and 3410 cm^{-1}, which were attributed to alkoxy C-O stretching, epoxy C–O stretching, O-H stretching (carboxyl), skeletal vibrations of the aromatic C=C bond, stretching vibrations of C=O in the carboxylic acid and carbonyl moieties, and O–H stretching vibrations (hydroxyl), respectively.[3-5] After reduction, the intensities of the stretching vibration bands of the oxide groups (O–H, C=O, and C–O) decreased significantly because GO was successfully reduced during the reduction reaction.[6, 7] The characteristics of C=O on the surface of GO (at approximately 1725 cm-1) were observed from GO and CGO-20. However, this peak disappeared in the FTIR spectra of CG20, suggesting a complete reduction of the GO in the CG20.

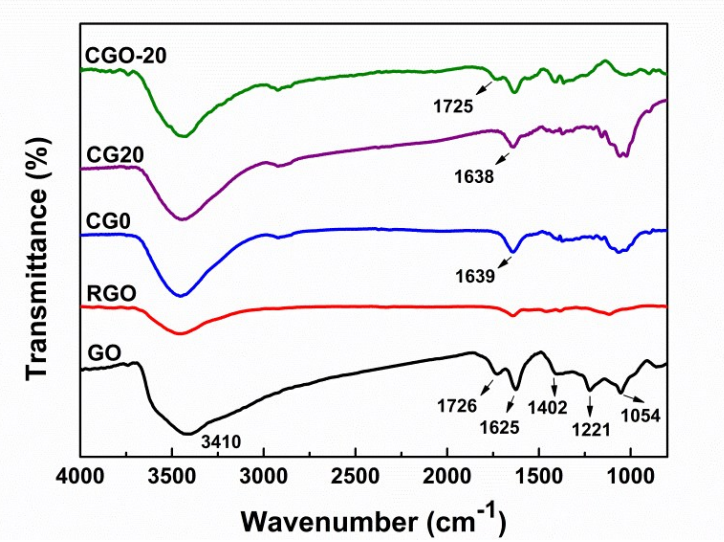

Figure S2. FTIR analysis spectra of GO, RGO, CG20, CG0 and CGO-20.

The XRD patterns of GO, RGO, and all of the hybrid films are shown in Figure S3. GO exhibited a characteristic diffraction peak (001) at 2θ = 10.2 °, which is correlated to an interlayer d-spacing of 8.62 Å.[8] After the reduction to graphene, a broad peak centered at 23.5 ° was observed in the XRD pattern of RGO, suggesting that the RGO nanosheets were loosely stacked in the obtained samples.[9, 10] For the neat NFC film, CG0, the pattern shows two broad reflection peaks at approximately 2θ = 15.2 ° and 22.3 ° between 5-40 °, which reveal a high degree-of-order in the cellulose Ⅰ structure.[11] However, the relatively low intensity of the main crystalline plane (at 22.3 °) may be due to the crystalline ordering of the cellulose Ⅰ allomorph that was slightly affected during the reduction of GO at the elevated temperature.[12-15] Moreover, after reduction, the typical peaks that correlated to the interlayer spacing of GO completely disappeared in the NFC/RGO hybrids, signifying a complete reduction of the GO in the NFC/GO

dispersion. The new diffraction peak of RGO overlapped with the peak of NFC, resulting in an increase in the intensity of the peak at 2θ = 23 °.

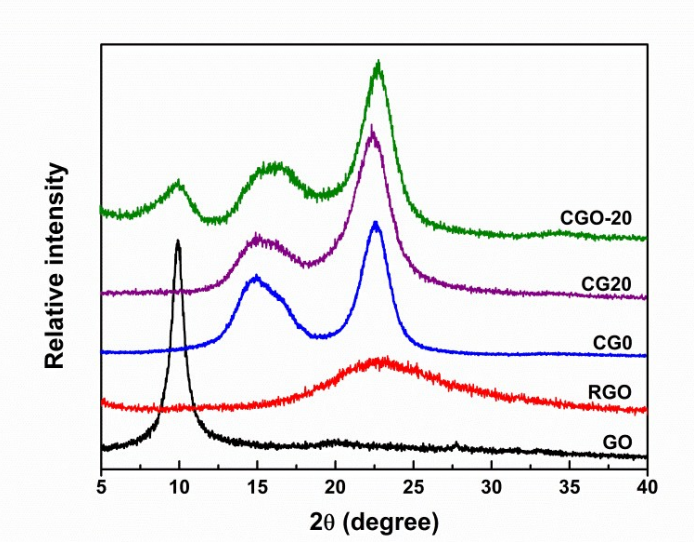

Figure S3. XRD patterns of GO, RGO, CGO, CG20, CG0-20.

To further confirm the reduction of GO in the hybrid films, the Raman spectrum was used to characterize the hybridized structure of the carbons in the graphene nanosheets (Figure S4). D bands (approximately 1330 cm^{-1}) and G bands (approximately 1590 cm^{-1}) were present in the Raman spectrum of GO, RGO, and the hybrid films. The D band is representative of sp^3-hybridized carbons in graphene nanosheets, whereas the G band corresponds to either edges or defects in the lattice.[16] The D/G intensity ratio [I(D/G)] of GO and RGO increased significantly from 1.01 to 1.33 after the reduction by hydrazine. The new graphitic domains created during the reduction were smaller than GO, which is attributed to the increase in the number of defects and edges in the graphitic lattice.[17, 18]

The Raman spectrum of the hybrid films was similar to that of RGO, and it possessed a higher I(D/G) than GO, suggesting the successful reduction of GO to RGO.

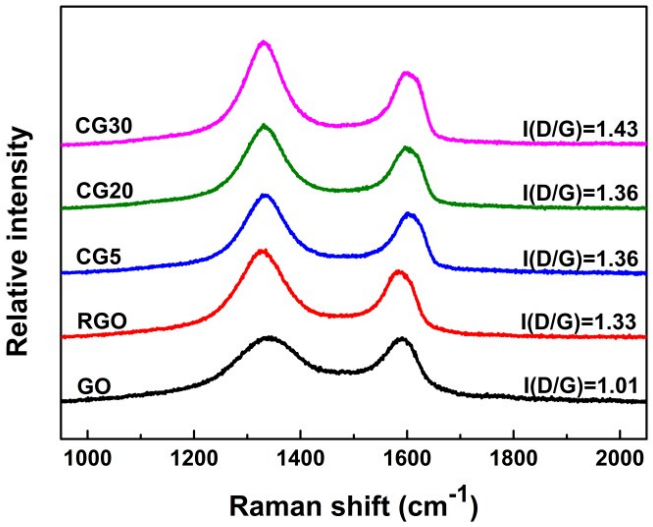

Figure S4. Raman spectrum of GO, RGO, and hybrid films with varied GO content.

Figure S5a illustrates the TGA curves of the samples. The small amount of mass loss of all of the samples below 100 °C is due to the volatilization of absorbed water. For GO, the curve displays a significant mass loss over a range of 150 to 250 °C due to the removal of oxygen-containing functional groups.[19, 20] In addition, only 11% mass loss was observed in the curve of RGO from 100 to 680 °C, indicating that most of the oxygen-containing functional groups were removed during the chemical reduction. Two steps of thermal degradation are observed in the DTG curve of CGO-20 from 100 to 600 °C (from 180-230 °C and from 230-400 °C), which are due to the thermal degradation of GO and NFC, respectively.[21, 22] The thermal degradation of CG20 began at approximately 230-390 °C, and in contrast to CGO-20, there was only one thermal degradation step

(Figure S5b). This revealed that there are few oxygen-containing groups on the graphene sheet after reduction in the hybrid dispersion, which is in agreement with the FTIR, XRD, and Raman data. Moreover, the RGO nanosheets enhanced the thermal stability of the hybrid films, considering that the CG20 exhibited a $T_{50\%}$ (temperature corresponding to 50% of weight loss) that was approximately 7 °C higher than that of CG0 ($T_{50\%}$ of CG20 was 327 °C, and $T_{50\%}$ of CG0 was 320 °C). Similar TGA curves can be easily obtained for other graphene/polymer composite materials, and the graphene-based composites typically exhibit improved thermal stability with a higher $T_{50\%}$ compared with neat matrices.[23, 24]

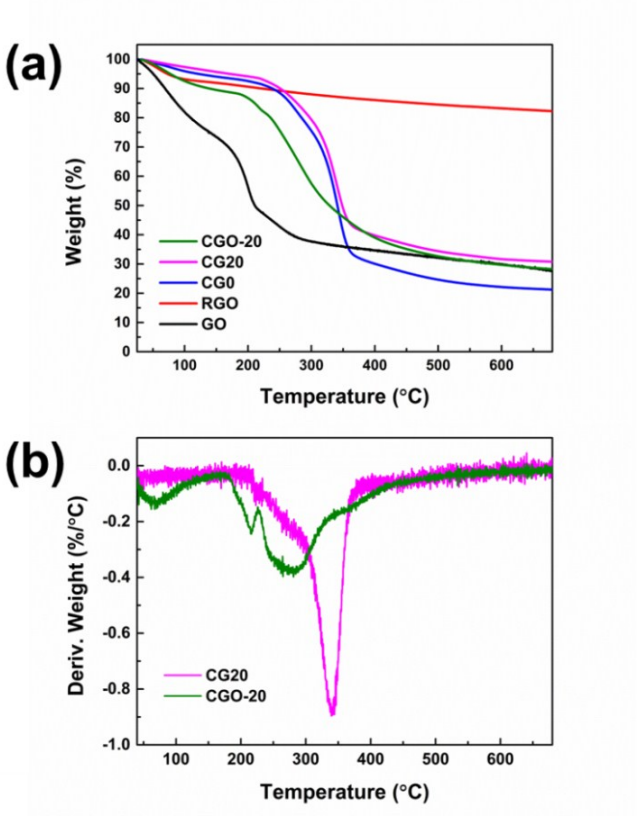

Figure S5. (a) TGA curves of GO, RGO, CG20, CGO-20, and CGO. (b) DTG curves of CG20, CGO-20.

4. The photographs of neat NFC and its hybrid films

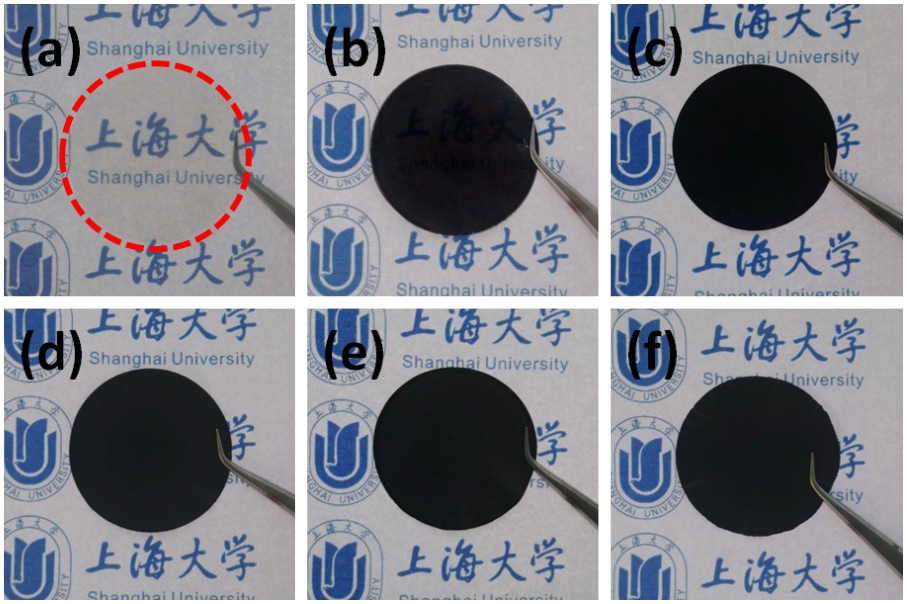

Figure S6. The photographs of (a) CG0. (b) CG0.5. (c) CG5. (d) CG10. (e) CG20. (f) CG30.

5. The cross-sectional SEM images of CG5

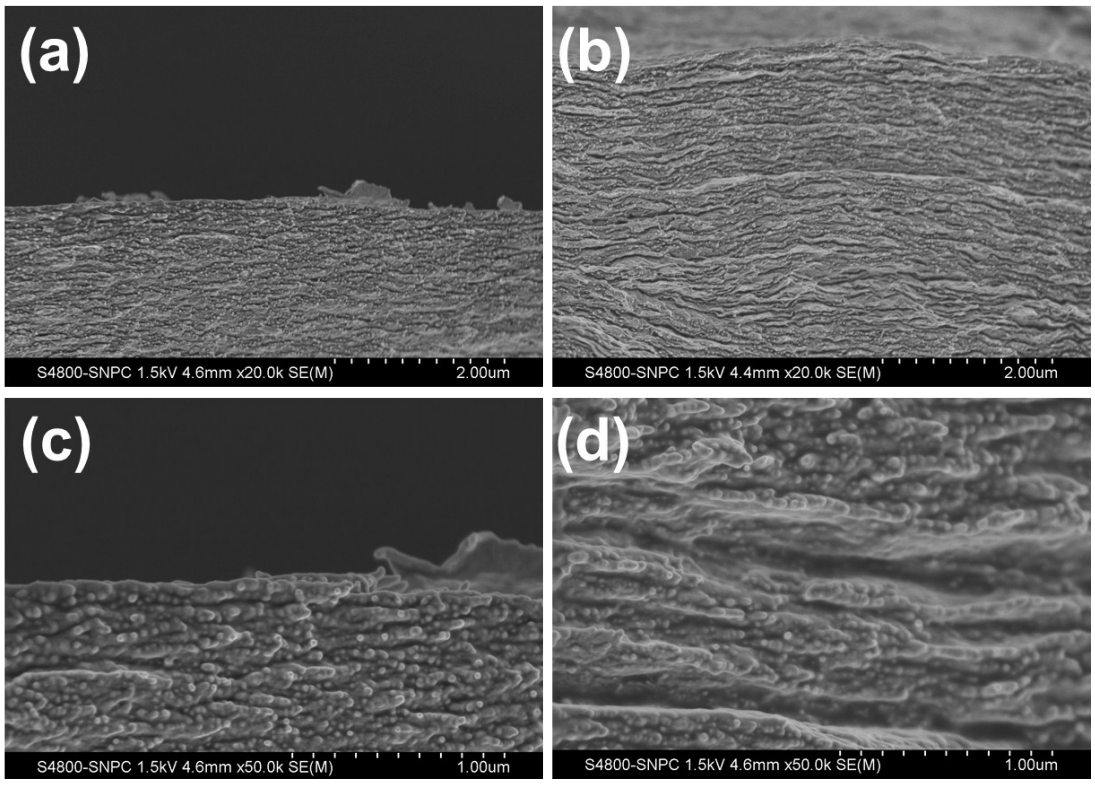

Figure S7. The cross-sectional SEM images of CG5 at magnifications of (a,b) 20,000× and (b,d) 50,000×

6. Theoretical calculation of the thermal conductivities at various orientation angles of the RGO nanosheets

EMA was modified to estimate the in-plane and through-plane thermal conductivities of the NFC/RGO hybrid films under various orientation degrees and was expressed as fullows:[25, 26]

$$K_{11}^{*} = K_{22}^{*} = K_m \frac{2 + f\left[\beta_{11}(1 - L_{11})\left(1 + \langle\cos^2\theta\rangle\right) + \beta_{33}(1 - L_{33})\left(1 - \langle\cos^2\theta\rangle\right)\right]}{2 - f\left[\beta_{11}L_{11}\left(1 + \langle\cos^2\theta\rangle\right) + \beta_{33}L_{33}\left(1 - \langle\cos^2\theta\rangle\right)\right]} \quad (1a)$$

$$K_{33}^{*} = K_m \frac{1 + f\left[\beta_{11}(1 - L_{11})\left(1 - \langle\cos^2\theta\rangle\right) + \beta_{33}(1 - L_{33})\langle\cos^2\theta\rangle\right]}{1 - f\left[\beta_{11}L_{11}\left(1 - \langle\cos^2\theta\rangle\right) + \beta_{33}L_{33}\langle\cos^2\theta\rangle\right]} \quad (1b)$$

with

$$\beta_{ii} = \frac{K_{ii}^{c} - K_m}{K_m + L_{ii}\left(K_{ii}^{c} - K_m\right)} \quad (2)$$

$$\langle\cos^2\theta\rangle = \frac{\int \rho(\theta)\cos^2\theta\sin\theta d\theta}{\int \rho(\theta)\sin\theta d\theta} \quad (3)$$

where K_{11}^{*}, K_{22}^{*} are the in-plane thermal conductivities, K_{33}^{*} is the through-plane thermal conductivity, θ is the angle between the materials plane and the local particles orientation plane, $\rho(\theta)$ is a distribution function describing the ellipsoidal particle orientation, f is the

volume fraction of the particles, K_{ii}^{c} (i =1, 2, 3) are the equivalent thermal conductivities along the symmetric axis of the aligned composites unit cells, K_m is the thermal conductivity of the matrix phase, L_{ii} are the geometrical factors dependent on the particle shape and are given by the following equation:

$$L_{11} = L_{22} = \frac{p^2}{2(p^2-1)} + \frac{p}{2(1-p^2)^{\frac{3}{2}}}\cos^{-1} p \quad \text{, for } p < 1 \tag{4}$$

$$L_{33} = 1 - 2L_{11} \tag{5}$$

$$K_{ii}^{c} = \frac{K_p}{1 + \frac{\gamma L_{ii} K_p}{K_m}} \tag{6}$$

with

$$\gamma = (1 + 2p)\alpha, \text{ for p} \leq 1 \tag{7}$$

Here a dimensionless parameter, α, is defined by

$$\alpha = \frac{R_{bd} K_m}{h} \tag{8}$$

where R_{bd} is thermal boundary resistance and h is the thickness of the RGO sheets.

For the laminate composites with the matrix containing the parallel RGO inclusion perpendicular to the X_3 axis (assuming an ideal case), $p \to 0$, $L_{11} = 0$ and $L_{33} = 1$. Thus, Eqs. (6) and (2) reduce, respectively, to the following expressions:

$$K_{11}^{c} = K_{22}^{c} = K_p \tag{9a}$$

$$K_{33}^{c} = \frac{K_p}{1 + \frac{\alpha K_p}{K_m}} \tag{9b}$$

and

$$\beta_{11} = \frac{K_p - K_m}{K_m} \tag{10a}$$

$$\beta_{33} = (1 - \alpha) - \frac{K_m}{K_p} \tag{10b}$$

Thus equations of EMA reduce to

$$K_{11}^{*} = K_{22}^{*} = K_m \frac{2 + f\left[\frac{K_p}{K_m}\left(1 + \langle \cos^2 \theta \rangle\right)\right]}{2 - \frac{w\rho_c}{\rho_g}\left[\frac{K_p h - K_m h - R_{bd} K_p K_m}{k_p h}\left(1 - \langle \cos^2 \theta \rangle\right)\right]} \tag{11}$$

$$K_{33}^{*} = K_m \frac{1 + f\left[\frac{K_p}{K_m}\left(1 - \langle \cos^2 \theta \rangle\right)\right]}{1 - f\left[\frac{k_p h}{h + R_{bd} K_p}\langle \cos^2 \theta \rangle\right]} \tag{12}$$

where K_m is the thermal conductivity of the matrix phase, K_p is the thermal conductivity of the laminated particle, f is the volume fraction of the particles, θ is the angle between the materials axis, X_3, and the local particles symmetric axis, R_{bd} is thermal boundary resistance, and h is the thickness of the RGO.

f can be calculated from the weight fraction:

$$f = \frac{w\rho_c}{\rho_g} \tag{13}$$

where w is the weight fraction of RGO in the composites, ρ_c is the density of the composites; ρ_g is the density of RGO.

For CG30, the K_p/K_m ratio was taken as approximately 4500 for the thermal conductivity of the RGO to NFC matrix, the R_{bd} values for graphene were 7.7×10^{-8} $K \bullet m^2 \bullet W^{-1}$,[27, 28] ρ_c can be measured by dividing the mass by the volume, ρ_g is widely accepted as 2.2 $g \bullet cm^{-3}$,[29] h is approximately 0.5 nm.[30]

In this study, AI = λ_X/λ_Z, and from this calculation, the theoretical AI was defined as K_{11}/K_{33} (or K_{22}/K_{33}).

Supplementing References

1 H. J. William S. and O. Richard E., *Journal of the Americal Chemical Society*, 1958, **80**, 1339-1339.

2 T. Saito, Y. Nishiyama, J. L. Putaux, M. Vignon and A. Isogai, *Biomacromolecules*, 2006, **7**, 1687-1691.

3 Y. Si and E. T. Samulski, *Nano Lett.*, 2008, **8**, 1679-1682.

4 I. K. Moon, J. Lee, R. S. Ruoff and H. Lee, *Nature communications*, 2010, **1**, 73.

5 Y. Feng, X. Zhang, Y. Shen, K. Yoshino and W. Feng, *Carbohydrate Polymers*, 2012, **87**, 644-649.

6 H. Tetsuka, R. Asahi, A. Nagoya, K. Okamoto, I. Tajima, R. Ohta and A. Okamoto, *Advanced Materials*, 2012, **24**, 5333-5338.

7 D. Li, M. B. Muller, S. Gilje, R. B. Kaner and G. G. Wallace, *Nature nanotechnology*, 2008, **3**, 101-105.

8 N. D. Luong, N. Pahimanolis, U. Hippi, J. T. Korhonen, J. Ruokolainen, L.-S. Johansson, J.-D. Nam and J. Seppälä, *Journal of Materials Chemistry*, 2011, **21**, 13991-13998.

9 M. C. Hsiao, S. H. Liao, M. Y. Yen, P. I. Liu, N. W. Pu, C. A. Wang and C. C. Ma, *ACS applied materials & interfaces*, 2010, **2**, 3092-3099.

10 S. Gambhir, E. Murray, S. Sayyar, G. G. Wallace and D. L. Officer, *Carbon*, 2014, **76**, 368-377.

11 T. Saito and A. Isogai, *Biomacromolecules*, 2004, **5**, 1983-1989.

12 H. Liimatainen, N. Ezekiel, R. Sliz, K. Ohenoja, J. A. Sirvio, L. Berglund, O. Hormi and J. Niinimaki, *ACS applied materials & interfaces*, 2013, **5**, 13412-13418.

13 H. Liimatainen, M. Visanko, J. A. Sirvio, O. E. Hormi and J. Niinimaki, *Biomacromolecules*, 2012, **13**, 1592-1597.

14 H. Liimatainen, T. Suopajarvi, J. Sirvio, O. Hormi and J. Niinimaki, *Carbohydr Polym*, 2014, **103**, 187-192.

15 T. T. T. Ho, T. Zimmermann, R. Hauert and W. Caseri, *Cellulose*, 2011, **18**, 1391-1406.

16 Y. Si and E. T. Samulski, *Chemistry of Materials*, 2008, **20**, 6792-6797.

17 C.-C. Teng, C.-C. M. Ma, C.-H. Lu, S.-Y. Yang, S.-H. Lee, M.-C. Hsiao, M.-Y. Yen, K.-C. Chiou and T.-M. Lee, *Carbon*, 2011, **49**, 5107-5116.

18 A. C. Ferrari, J. C. Meyer, V. Scardaci, C. Casiraghi, M. Lazzeri, F. Mauri, S. Piscanec, D. Jiang, K. S. Novoselov, S. Roth and A. K. Geim, *Physical Review Letters*, 2006, **97**, 187401-187404.

19 Y. W. Zhu, M. D. Stoller, W. W. Cai, A. Velamakanni, R. D. Piner, D. Chen and R. S. Ruoff, *Acs Nano*, 2010, **4**, 1227-1233.

20 K. Zhang, L. L. Zhang, X. S. Zhao and J. Wu, *Chemistry of Materials*, 2010, **22**, 1392-1401.

21 M. Yadav, K. Y. Rhee, I. H. Jung and S. J. Park, *Cellulose*, 2013, **20**, 687-698.

22 H. Fukuzumi, T. Saito, T. Wata, Y. Kumamoto and A. Isogai, *Biomacromolecules*, 2009, **10**, 162-165.

23 N. Yousefi, X. Lin, Q. Zheng, X. Shen, J. R. Pothnis, J. Jia, E. Zussman and J.-K. Kim, *Carbon*, 2013, **59**, 406-417.

24 N. Song, J. Yang, P. Ding, S. Tang, Y. Liu and L. Shi, *Industrial & Engineering Chemistry Research*, 2014, **53**, 19951-19960.

25 C.-W. Nan, R. Birringer, D. R. Clarke and H. Gleiter, *Journal of Applied Physics*, 1997, **81**, 6692-6699.

26 Q. Li, Y. Guo, W. Li, S. Qiu, C. Zhu, X. Wei, M. Chen, C. Liu, S. Liao, Y. Gong, A. K. Mishra and L. Liu, *Chemistry of Materials*, 2014, **26**, 4459-4465.

27 C. Faugeras, B. Faugeras, M. Orlita, M. Potemski, R. R. Nair and A. K. Geim, *Acs Nano*, 2010, **4**, 1889-1892.

28 D. Konatham, D. V. Papavassiliou and A. Striolo, *Chemical Physics Letters*, 2012, **527**, 47-50.

29 D. Wang, T. Zhou, J.-W. Zha, J. Zhao, C.-Y. Shi and Z.-M. Dang, *Journal of Materials Chemistry A*, 2013, **1**, 6162-6168.

30 N. Song, J. Yang, P. Ding, S. Tang and L. Shi, *Composites Part A: Applied Science and Manufacturing*, 2015, **73**, 232-241.